SANDIA REPORT SAND84—1729 • Unlimited Release • UC—34
Printed December 1984

Dynamic Shock Studies of PZT 95/5 Ferroelectric Ceramic

L. C. Chhabildas

Prepared by
Sandia National Laboratories
Albuquerque, New Mexico 87185 and Livermore, California 94550
for the United States Department of Energy
under Contract DE-AC04-76DP00789

Issued by Sandia National Laboratories, operated for the United States Department of Energy by Sandia Corporation.

Printed in the United States of America
Available from
National Technical Information Service
U.S. Department of Commerce
5285 Port Royal Road
Springfield, VA 22161

NTIS price codes
Printed copy: A03
Microfiche copy: A01

Distribution
Category UC34

SAND84-1729
Unlimited Release
Printed December 1984

Dynamic Shock Studies of PZT 95/5 Ferroelectric Ceramic

L.C. Chhabildas
Thermomechanical & Physical Division
Sandia National Laboratories
Albuquerque, New Mexico 87185

ABSTRACT

Using gas gun and velocity interferometric techniques, the shock loading, the shock release, and the pressure-shear response of 95/5 PZT ferroelectric ceramic have been determined up to 4.6 GPa. Results of these experiments indicate that the material undergoes a phase transformation at 0.5 GPa under dynamic loading conditions. Experiments over the stress region 0.9 to 2.6 GPa indicate that the material is in a mixed phase, with the concentration of the FE phase diminishing with increasing stress. The kinetics of pore compaction and crush-up behavior dominate the mechanical material response above 2.6 GPa. Results of pressure-shear experiments in combination with that of release wave experiments suggest that dynamic yielding initiates at 0.5 GPa, the pressure at which FE to AFE phase transformation also begins.

Acknowledgements

The author wishes to acknowledge R. H. Dungan and W. D. Williams for providing the samples for shock studies. Sincere thanks to D. J. Holcomb and D. D. Bloomquist for allowing access to their unpublished data on static and dynamic tests, respectively. Many special thanks to J. M. Miller and R. D. Hardy for their assistance in conducting these experiments.

Contents

Figures

Tables

1 Introduction

Ferroelectric materials with a stress-induced ferroelectric-to-antiferroelectric (FE-to-AFE) phase transformation are of interest because of their use in shock-actuated power supplies[1]. PZT 95/5 is one such ceramic; its composition is such that its phase boundary is located around 0.3 GPa[2] at room temperature. Hydrostatic compression induces the transformation [3,4], thereby destroying any polarization and releases the associated surface charge[5,6]. It is this phenomenon that forms the basis of a shock-actuated power supply.

In this paper, we report experimental results describing the shock loading, the shock release, and the pressure-shear response of the material up to 4.6 GPa. These experiments were performed to obtain a good dynamic mechanical description of the material. Although there has been considerable attention devoted to the material, studies describing its dynamic shock-compression [7-10] behavior are scarce. With recent developments in both diagnostic and loading techniques [11], refined time-resolved measurements can be performed to determine the shock-compression behavior accurately. These results would also be useful in developing constitutive relations to describe its dynamic mechanical behavior more generally. The lack of accurate shock-compression results has impeded the development of constitutive relations for the material. This report is limited to description of results pertaining to the dynamic stress-strain response of unpoled virgin materials. This is considered to be the first step in arriving at a general constitutive relation to represent the material, which eventually would also include coupled electro-mechanical response of the poled material.

Results of these experiments indicate that the material undergoes a phase change at 0.5 GPa under dynamic loading conditions. Up to 0.5 GPa in the ferroelectric (FE) phase, its stress-strain behavior is anomalous, i.e., the sound speed decreases with increasing stress. Experiments over the stress region 0.9 to 2.6 GPa indicate that the material is in a mixed phase, with the concentration of FE phase diminishing with increasing stress. The kinetics of pore compaction and crush-up behavior dominate the mechanical material response above 2.6 GPa. Results of pressure-shear experiments, when combined with shock release experiments, suggest that dynamic yielding initiates at 0.5 GPa, the pressure at which the FE-to-AFE phase transformation begins.

In the following section, the experimental technique used to obtain shock loading and pressure-shear loading conditions is described. The results of these experiments are reported and discussed in subsequent sections.

2 Experimental Technique

2.1 Uniaxial-Strain Loading Technique

The experimental arrangement used to obtain uniaxial-strain loading conditions [12] is depicted in Figure 1(a). Fused silica [13] impactors backed by a low-density carbon foam were made to impact ferroelectric specimens which had laser interferometer windows bonded to them. The window materials used in this investigation were fused silica or Z-cut sapphire single crystals [13]. The impact conditions are summarized in Table 1. The impact conditions were such that stress levels of 0.9 GPa to 4.6 GPa were obtained in the ferroelectric specimens.

Table 1. Summary of Experiments

Shot No.	Sample Density (gm/cc)	Sample Thick. (mm)	Impactor Thick./Matl (mm)/(a)	Impact Velocity (km/s)	Ultrasonic Wave Speed Long. (km/s)	Shear (km/s)	Type Expt. (b)
FER2	7.269	1.961	3.30/FS	0.250	4.196	2.541	RL
FER3	7.265	1.958	3.30/FS	0.361	4.183	2.538	RL
FER4	7.295	2.907	3.31/FS	0.111	4.184	2.532	RL
FER5(c)	7.330	1.965	1.02/FS	0.349	---	---	RL
FER6	7.336	3.121	4.32/AL_2O_3	0.315	4.188	2.526	RL
FES1	7.328	2.975	12.8/AL	0.151	4.168	2.521	PS
FES2	7.337	2.960	12.7/AL	0.187	4.186	2.531	PS
FES5	7.317	2.981	9.6/AL	0.328	4.180	2.519	PS

a. AL, AL_2O_3, and FS represent 6061-T6 aluminun, z-cut sapphire, and fused silica, respectively, for impactor materials.

b. PS represents pressure-shear experiment; RL represents release experiment.

c. Experiment performed by Doug Bloomquist.

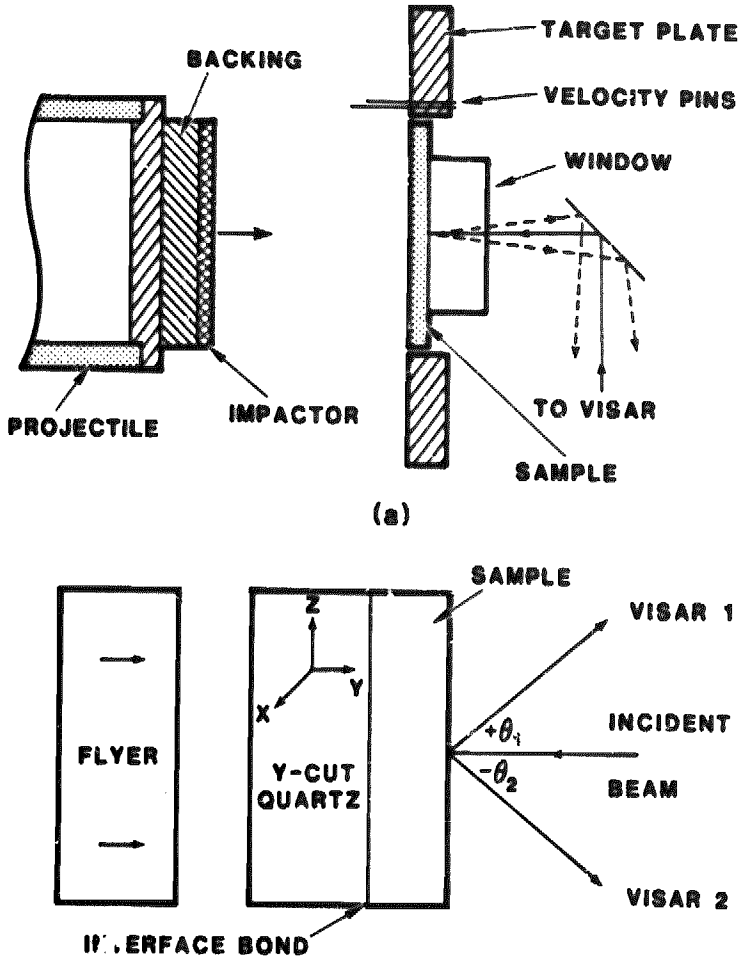

Figure 1. Experimental impact configuration to achieve a) uniaxial-strain loading conditions and b) pressure-shear loading conditions.

The projectiles were accelerated to the desired velocities on the single-stage compressed gas gun [14]. The projectile velocity was determined by measuring the transit time of the projectile between two precisely spaced charged pins located on the target plate, and was measured to an accuracy of 0.2% . Impact tilt was determined by measuring the simultaneity of the projectile surface arrival at an array of co-planar charged pins located on the target plate. The average tilt for these series of shots was determined to be less than 0.5 mrad.

The particle velocity history at the sample-window interface was measured using a velocity interferometer [15] identified by the acronym, VISAR. The VISAR has been described previously and only the relevant features will be mentioned here. Fringes are produced in the interferometer by superimposing the light reflected from the target at any time with the light that was reflected earlier in time by the delay time in the interferometer. The delay time, τ, was introduced by using either glass etalons [15] or a lens combination [16] in the delay leg of the interferometer. The resulting number of fringes, $F(t)$, produced in the interferometer is related to the velocity of the reflecting surface by

$$u(t - \frac{1}{2}\tau) = \frac{\lambda}{2\tau} \frac{F(t)}{(1+\delta)(1+\Delta\nu/\nu)} \tag{1}$$

where λ is the wavelength of the light used(514.5 nm). δ is a correction term due to the wavelength dependence of the refractive index of the etalon material [17]. $\delta = 0.034$ when etalons are used to achieve the necessary delay, or 0 when a lens combination is used to obtain the required delay time. The optical correction term $\Delta\nu/\nu$ results from the change in refractive index of the window material with shock stress. $\Delta\nu/\nu$ is 0.06 for fused silica and 0.77 for Z-cut sapphire single crystals [13].

2.2 Pressure-Shear Loading Technique

The technique used to generate one-dimensional pressure-shear waves [18] in the ferroelectric specimens is depicted in Figure 1(b). As indicated in the diagram, a projectile impacts a Y-cut quartz crystal that has a sample bonded to its rear surface. The projectiles are accelerated to the desired impact velocities using a single-stage compressed gas gun. Owing to the anisotropic structure of crystalline quartz, a pure longitudinal wave cannot propagate along its Y-axis [19-21]. Upon normal impact of Y-cut quartz, a two-wave structure is generated with both waves having particle-velocity changes in both the longitudinal and transverse directions, i.e. the crystallographic Y and Z axes of the crystal. The fast wave, denoted as a quasilongitudinal (QL) wave, has particle-velocity changes primarily in the longitudinal direction, while the slow wave, denoted as a quasitransverse (QT) wave, has particle-velocity changes primarily in the transverse direction. These waves are shown as QL and QT in Figure 2(a), and, as indicated, they lie in the crystallographic Y-Z plane. By controlling the thickness of the Y-cut quartz generator, the arrival time of the QT wave relative to the QL wave can be varied. The stress pulse input at the bonded interface is indicated in Figure 2(b).

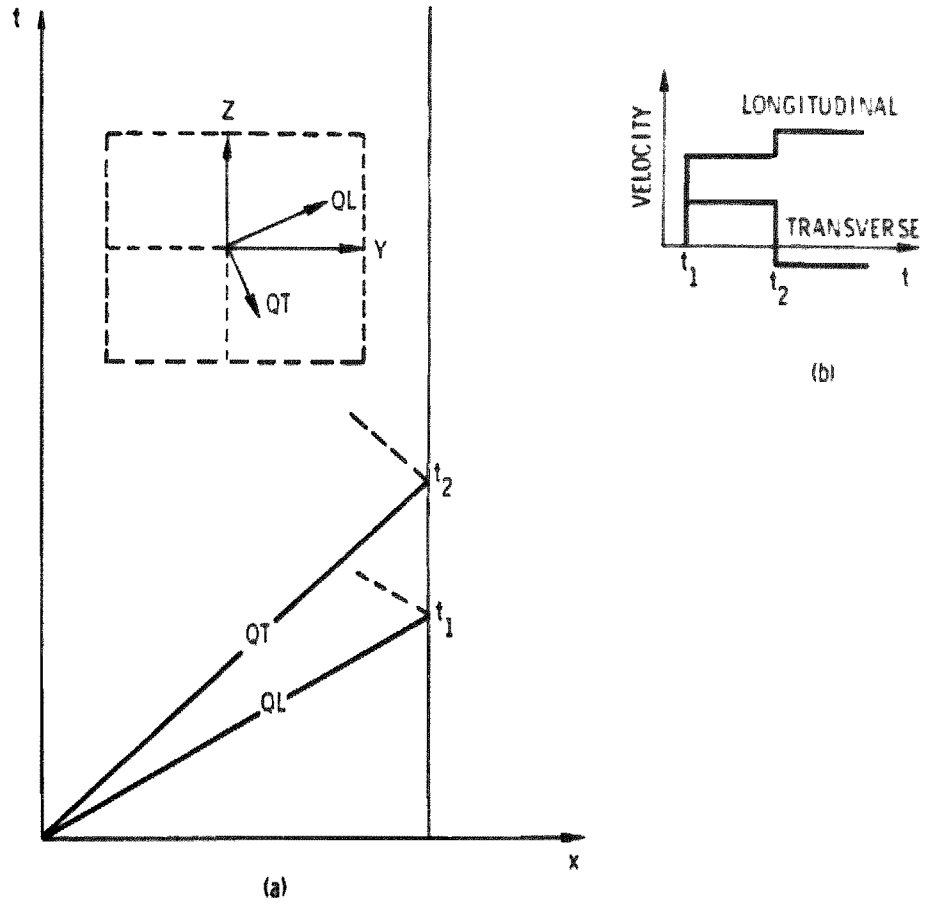

Figure 2. Response of Y-cut quartz to normal impact loading. A Lagrangian x-t diagram depicting the arrival of QL and QT waves at the bonded interface is indicated in a), while the longitudinal and transverse stress pulse input at the bonded interface is indicated in b).

Upon arrival of the QL wave at the interface, the sample is simultaneously loaded in compression and shear. The magnitudes of the particle-velocity changes associated with the arrival of the compression wave and shear wave at the free surface are determined

using two velocity interferometers, VISARs, as indicated in Figure 1(b). By using one incident beam and monitoring two reflected beams at angles $+\theta_1$ and $-\theta_2$, the longitudinal velocity $U(t)$ and the transverse velocity $V(t)$ can be determined simultaneously [20]. This is possible because the velocities measured by the two interferometers are related to $U(t)$ and $V(t)$ by

$$u(+\theta_1, t) = \frac{1}{2}U(t)(1 + cos\theta_1) + \frac{1}{2}V(t)sin\theta_1, \tag{2}$$

and

$$u(-\theta_2, t) = \frac{1}{2}U(t)(1 + cos\theta_2) - \frac{1}{2}V(t)sin\theta_2. \tag{3}$$

The velocity $u(\theta, t)$ measured by each interferometer is related to the number of fringes $F(t)$ by the relation in Equation (1). $\Delta\nu/\nu$ is zero in Equation (1), as the measurements are made at the free surface.

Reflected beams at θ_1 and $-\theta_2$ from the incident beam can be obtained by preferentially scratching the reflecting mirror on the free surface of the ferroelectric specimen. Care was taken, however, to ensure that these marks were perpendicular to the plane of transverse wave propagation.

2.3 Material Preparation

The material was prepared by intimately mixing lead oxide, zirconium dioxide, titanium dioxide, and niobium pentoxide in the amounts determined by the atomic formula:

$$Pb_{.9897}Nb_{.0206}(Zr_{.96}Ti_{.04})_{.9794}O_3$$

The powder mixture was calcined at 1000°C to react the constituent oxides into a solid solution of lead zirconate-lead titanate-lead niobate, generally called 95/5 PZT.

The calcined PZT powder was wet-milled to an average particle size of about two microns and then oven dried. Organic binders were added to the powder to promote dry pressing. At the same time, 0.8 weight percent of 100 micron lucite spheres were added to control the final fired density. The resulting powder mixture was pressed into billets approximately 1 cm × 3 cm × 5 cm by placing the powder in a suitable steel die and applying a pressure of 70 MPa. The billets were bisque-fired at a temperature of 700°C in an air atmosphere to remove the organic binders and lucite spheres. The bisqueware, along with atmosphere control powder of the same composition, was placed in a tightly closed sagger and then sintered at 1350°C for six hours, after which it was cooled gradually over a period of seventy-two hours. During the final stages of cooling, a cooling rate of 5°C per hour is usually necessary to induce the FE phase.

Test specimens in the form of 25-mm diameter discs were machined from the billets using standard techniques for processing brittle ceramic materials. The faces were lapped and polished while maintaining parallelism to 25 μm. A detailed description of material preparation is given in Reference 22.

3 Results And Discussion

The impact conditions for the series of experiments performed in the ferroelectric specimens to determine dynamic mechanical properties are listed in Table 1. The series of experiments, denoted by FER, refer to shock-loading, followed by release, while FES, refer to pressure-shear loading experiments. The interface particle-velocity histories for shots FER2, FER3, and FER4 are shown in Figure 3, and shots FER5 and FER6 are shown in Figure 4. The longitudinal and transverse free-surface velocity profiles obtained in pressure-shear experiments FES1, FES2, and FES5 are indicated in Figures 5, 6, and 7, respectively.

The experimentally-measured interface-velocity histories can be used to determine the stress, strain, wave velocity, and the material velocity behind the shock front, *i.e.* the Hugoniot states of the material. These are discussed in detail in the following section.

3.1 Hugoniot States

By correlating the impact time with wave arrival times, the wave velocity of the loading wave profiles can be determined. The two main sources of error in estimating the wave arrival times are: (i) the impact misalignment between the target and the impactor (tilt), and (ii) the uncertainty in determining the wave arrival on the records. Since relatively thin specimens were used in this investigation, the uncertainty of the wave velocity is $\pm 2\%$. The wave velocity of the leading edge of the wave is tabulated in Table 2. Using impedance matching techniques, the particle velocities measured at the sample-window interface were corrected to obtain the material particle velocity (the Hugoniot particle velocity) behind the shock front, and are also reported in Table 2.

Table 2. Results Of Shock-Loading Experiments.

Shot No.	Wave Speed Toe (a) (km/s)	Wave Speed Half-Amplitude (km/s) (b)	Particle Velocity (km/s)	Shock Stress (GPa)	Shock Strain	Release(c) Wave-Speed (km/s)	Shear-Wave Speed
FER2	4.19	3.43	.08249	2.095	0.02369	4.96/4.84	
FER3	4.16	3.66/(1.77)(d)	.12100	2.900	0.04096	5.40/5.18	
FER4	(e)	2.85	.0404	0.939	0.01324	5.02/4.95	
FER5	- - -	3.65/(2.80)(d)	.114(f)	2.82(f)	0.0356(f)	5.15(g)	
FER6	4.07	3.72/(2.25)(d)	.212(f)	4.60(f)	0.077 (f)	5.01(g)	
FES1	4.07	3.06	.0458	1.11	0.0143		2.76
FES2	4.26	3.21	.0535	1.34	0.0159		2.61
FES5	4.15	3.60	.0685	2.48	0.0274		2.58

a. These are measured wave speeds for the toe of the leading wave.

b. These estimates for the half-amplitude of the second elastic wave are based on a velocity of 4.18 km/s for the toe of the leading wave.

c. These represent the initial Lagrangian/Eulerian release wave velocity.

d. These wave speeds in parentheses are for the crush-up wave or the third wave. The material begins to crush at stresses over 2.6 GPa.

e. No fiducial recorded on this shot.

f. Based on impact conditions, these should be the end states.

g. Since the wave is attenuated, the release wave speed estimate is a lower bound. The Lagrangian wave speed only is reported.

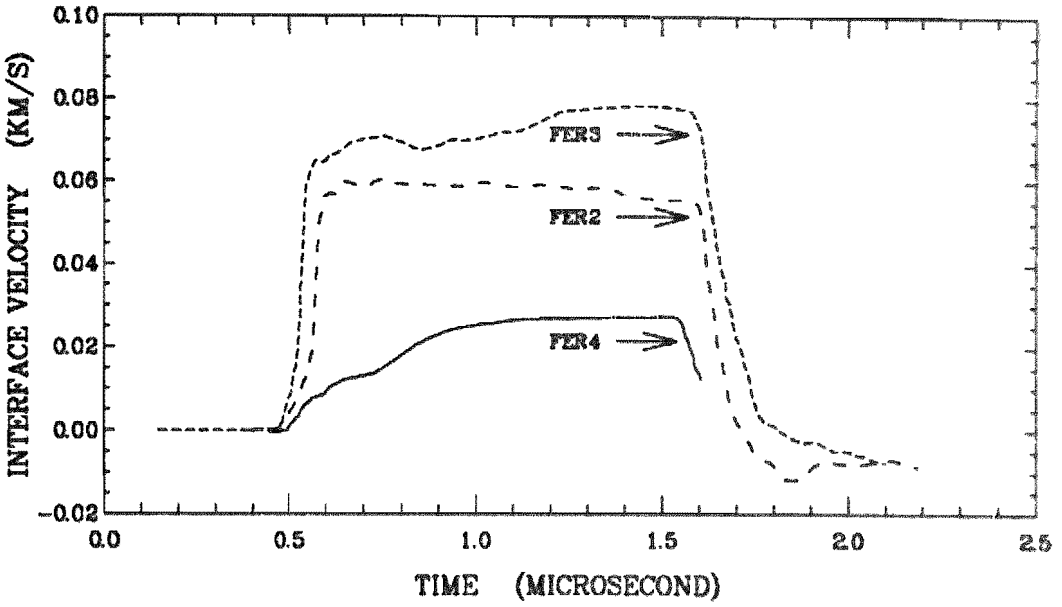

Figure 3. Shock loading and release profiles for shots FER2, FER3, and FER4 measured at the ferroelectric sample and sapphire window interface. The wave arrival time for shot FER4 has been translated by -0.20 μs to display them on the same graph.

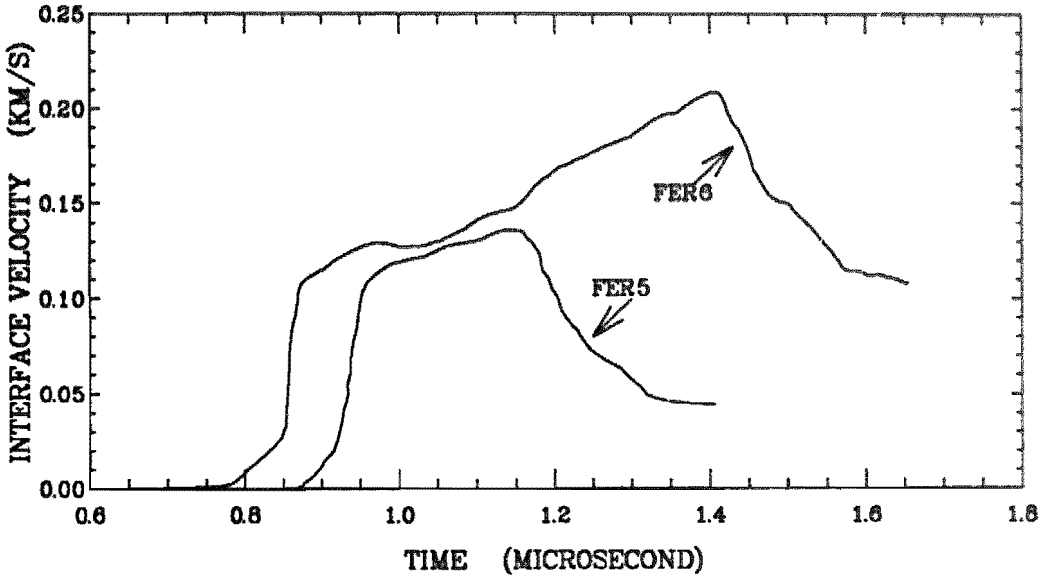

Figure 4. Shock loading and release profiles for shots FER5 and FER6 measured at the ferroelectric sample and fused silica window interface. The wave arrival time for shot FER5 has been translated by 0.4 μs.

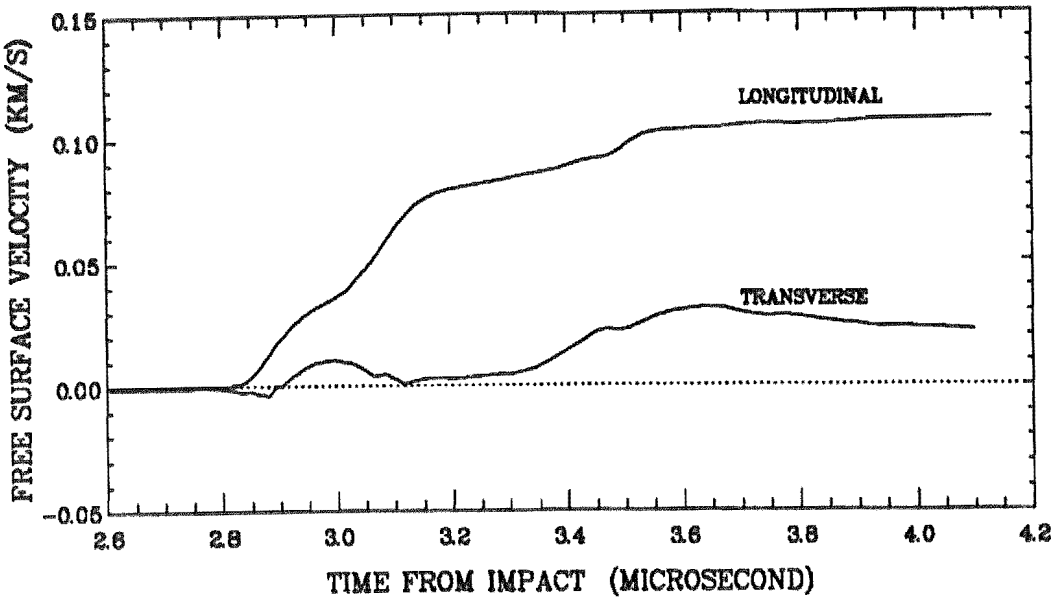

Figure 5. Measured longitudinal and transverse free-surface velocity profiles for the pressure-shear loading configuration in experiment FES1.

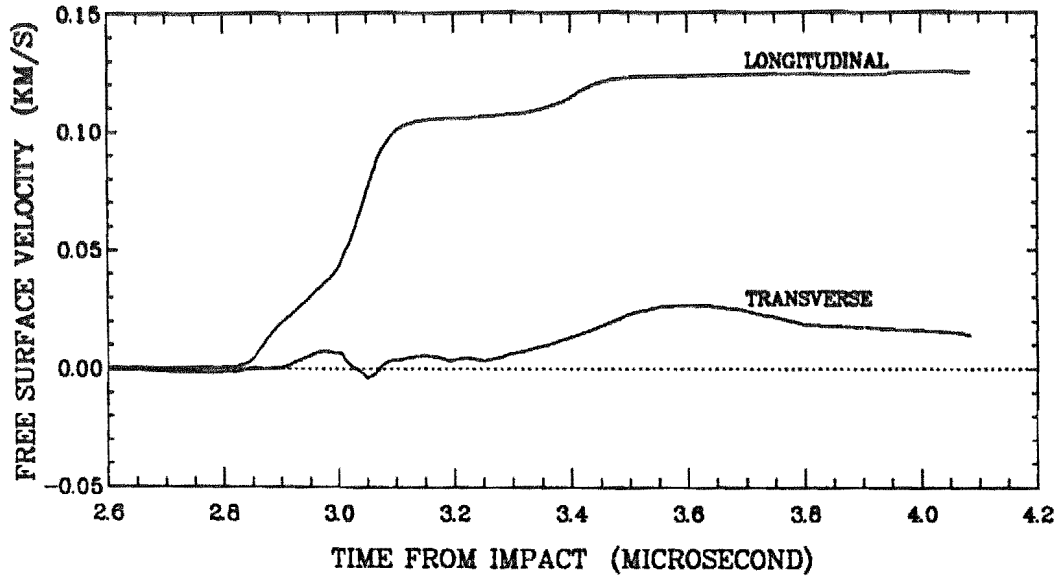

Figure 6. Measured longitudinal and transverse free-surface velocity profiles for the pressure-shear loading configuration in experiment FES2.

Generally, the loading wave profiles for the shocked ferroelectric consist of a two-wave structure when shocked below 2.6 GPa, and a three-wave structure when the material is shocked above 2.6 GPa. The first wave is a ramp wave, loading the material up to approximately 0.5 GPa. This is followed by a second wave, whose wave velocity and rise time are dependent on the stress amplitude for stresses to approximately 2.6 GPa. Two-wave structures observed upon dynamic loading of materials are usually indicative of a cusp in the Hugoniot due either to (i) a phase transformation or (ii) dynamic yielding in the material. The cusp at 0.5 GPa is believed to be due to both dynamic yielding and the onset of the FE-to-AFE phase change.

In Figure 8, the variation of wave velocity *vs* particle velocity is illustrated for shock experiments conducted below 2.6 GPa. Since there is a finite risetime associated with wave propagation, the shock wave speeds listed in Table 2 are measured at the mid-point of the second wave. The behavior of the second wave is reminiscent of a plastic wave, in that the wave steepens as the stress amplitude increases. Above 2.6 GPa, an additional wave structure develops (Figure 9), and is due to the kinetics of the dynamic pore-compaction process. In particular, due to the sluggish nature of the pore-compaction process (as evidenced by finite compaction risetimes), the peak stress in experiments FER5 and FER6 is attenuated before the stre. ; wave arrives at the plane of measurement.

The longitudinal and transverse free-surface velocity measurements from pressure-shear experiments are indicated in Figures 5, 6, and 7. These experiments correspond to longitudinal stress states of 1.10, 1.34, and 2.48 GPa, respectively. As shown in these figures for the longitudinal wave, a ramp wave followed by a shock is observed in all three experiments, similar to the features observed in shock-loading and release experiments discussed above. The reshock wave observed is due to the characteristic of the Y-cut quartz crystal buffer. [See Figure 2(b).] The reshock wave is not distinct for the experiment at 2.48 GPa in Figure 7. Due to the sluggish nature of the pore-compaction wave, the reshock wave is dispersed and expected to arrive late.

The Lagrangian shock-velocity *vs* particle-velocity data, tabulated in Table 2, are shown plotted in Figure 10. As indicated in the figure, the shock velocity of the material decreases initially with particle velocity. Although no specific measurements were performed over this particle velocity range, the wave-velocity *vs* particle-velocity profiles indicated in Figures 8 and 9, suggest the response of the material is uniform and reproducible over this particle-velocity region. The variation observed in Figures 8 and 9 in this particle-velocity range corresponds to that of a timing error of approximately 6 ns, which is well within the experimental uncertainty. Since the leading edge of the wave is traveling at approximately 4.18 km/s, it also indicates that the initial wave is elastic; and because the waves overlay, it is centered. The behavior of shock velocity *vs* particle velocity for the second wave is also shown in Figure 10. The cluster of poi..s at a particle velocity of 0.10 km/s, indicates the onset of pore-compaction. The shock velocities indicated in Figure 10 at particle velocities greater than 0.10 km/s are those of the third wave, the pore-compaction wave. Since the pore-compaction wave is attenuated in experiments FER5 and FER6, the center of the wave is not very well defined, and has been estimated from

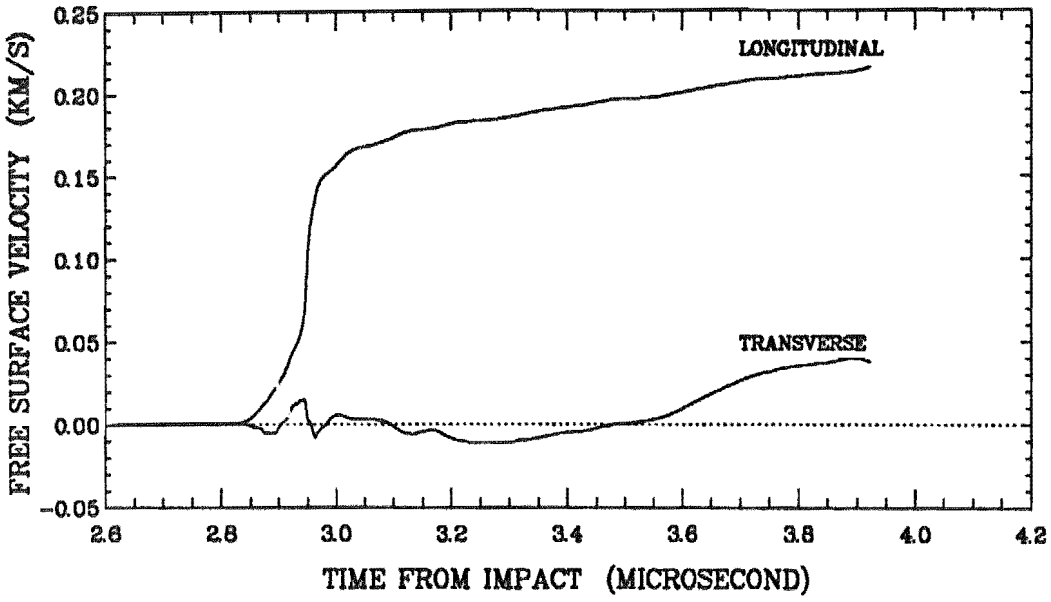

Figure 7. Measured longitudinal and transverse free-surface velocity profiles for the pressure-shear loading configuration in experiment FES5.

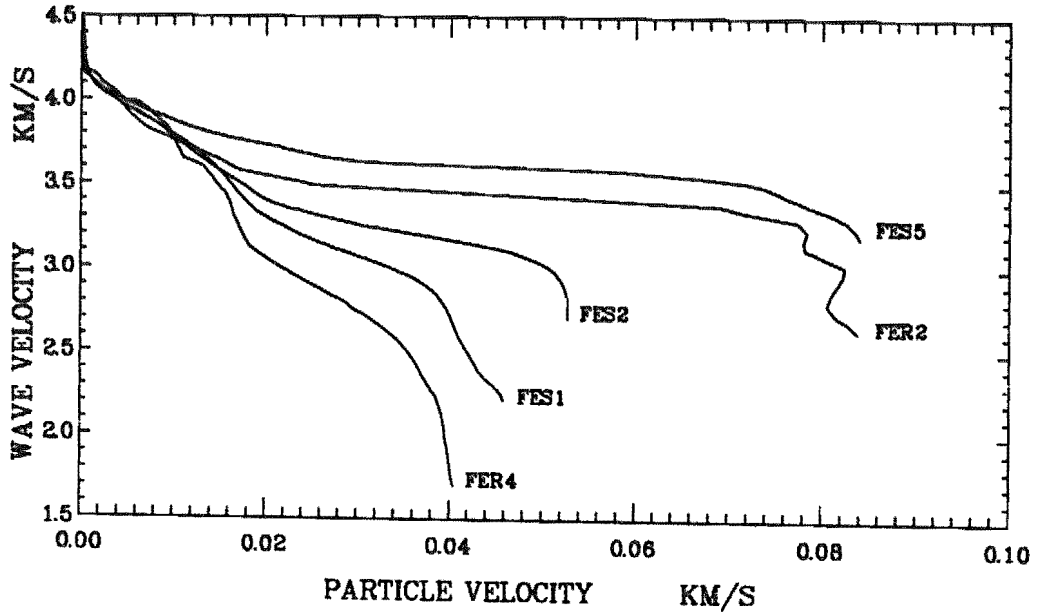

Figure 8. The variation of wave velocity vs particle velocity illustrated for shock experiments below 2.6 GPa. A two-wave structure is indicated.

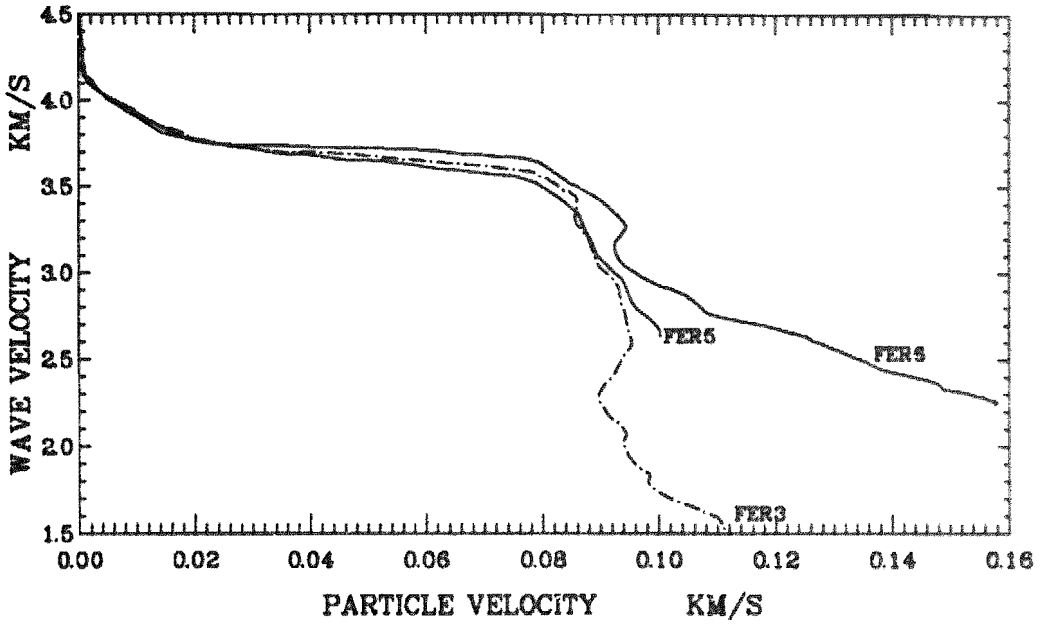

Figure 9. The variation of wave velocity *vs* particle velocity for shock experiments above 2.6 GPa. A three-wave structure is indicated.

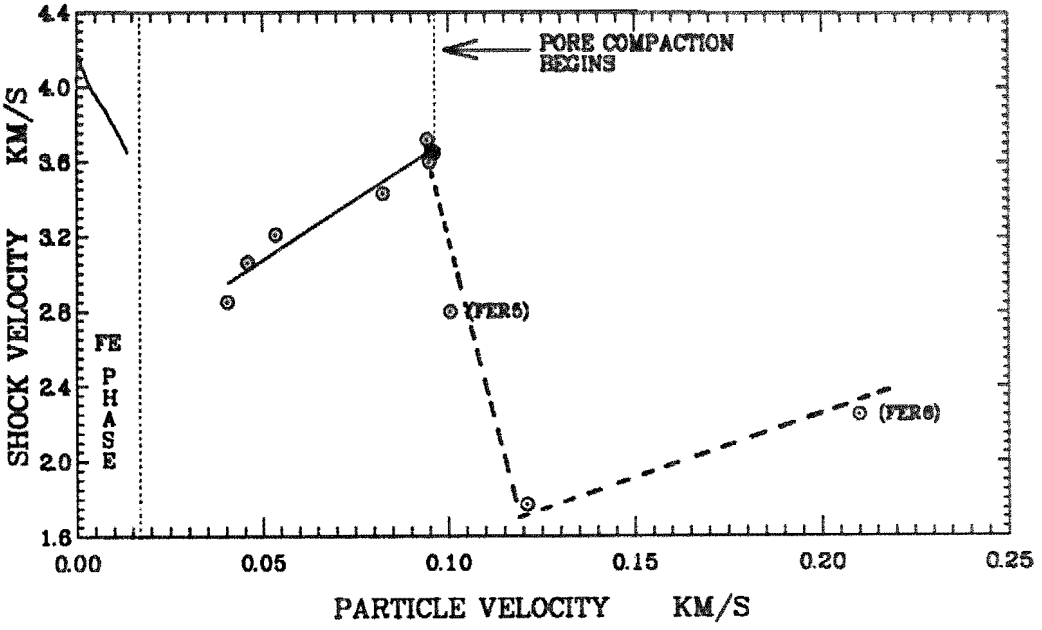

Figure 10. Shock velocity *vs* particle velocity variation for PZT 95/5 as determined from these experiments.

the known impact conditions. A linear least squares fit to the data for the *second wave* yields

$$U_s = 2.43 + 12.84u_p, \tag{4}$$

where U_s is the shock velocity of the second wave at a particle velocity of u_p, in units of km/s. [If a linear least squares fit is performed to the data for the second wave in the form $(U_s - u_e) = C_o + s(U_p - u_e)$ then the coefficients, u_e, C_o, s are 0.015 km/s, 2.61 km/s, and 12.84, respectively. This relation takes into consideration that a two wave structure exists for the material, and u_e is the particle velocity amplitude of the first wave.]

An incremental analysis [23] given by the equations

$$\sigma = \sum \rho_o c du, \text{ and } \eta = \sum du/c, \tag{5,6}$$

was used to estimate the peak shock stress and strain, where σ and η are the shock stress and strain upon loading, ρ_o is the initial density of the material, and c is the Lagrangian wave velocity of the wave for the corresponding increment du. This assumes that the measured wave profiles are centered. No attempt was made to verify this assumption experimentally. For shots FER5 and FER6, where the measured wave profiles are attenuated due to a sluggish compaction process, shock jump conditions were used above the attenuated stress state to estimate the final Hugoniot states. These stress and strain states are tabulated in Table 2 and are shown plotted in Figure 11. The results of hydrostatic stress-strain experiments on porous ($\rho = 7.3$ gms/cm^3) [4] and solid ($\rho = 7.96$ gms/cm^3) [24] PZT 95/5 ferroelectric material, are also indicated in Figure 11.

3.2 Release States

Also shown in Figures 3 and 4 are the release profiles obtained in these experiments. The particle velocity decrease indicated in the figures is a measure of the release states for the material. The negative particle velocity measured for experiments FER2 and FER3 can be explained with the aid of a Langragian x-t and a corresponding p-u diagram. This is illustrated for experiment FER2 in Figure 12. As indicated in the diagram, upon impact a stress wave propagates both into the material and the impactor. This is indicated as state 1. Upon arrival of the stress wave at the sample-window interface, the material will shock up to state 2. Since sapphire is a higher impedance material, the reshock wave will reflect into the material. The sample dimension in experiments FER2 and FER3 is such that the reflected reshock wave arrives at the impactor-sample interface before the release wave emanating from the far side of the impactor does. Due to wave interactions at the impactor-sample interface, the material will release from state 2 to state 3, as indicated in the p-u diagram. Note that the material prior to release is at state 3 which is a higher stress state but at a lower particle velocity when compared to state 1. This is also indicated as a particle velocity decrease in experiment FER2 (Fig. 3) prior to the arrival of the main release wave. A particle velocity decrease (similar to that seen in FER2) is not evident for experiment FER3, due to the arrival of the pore compaction wave. The release wave now propagates into a material which is at state 3, and, as indicated in the

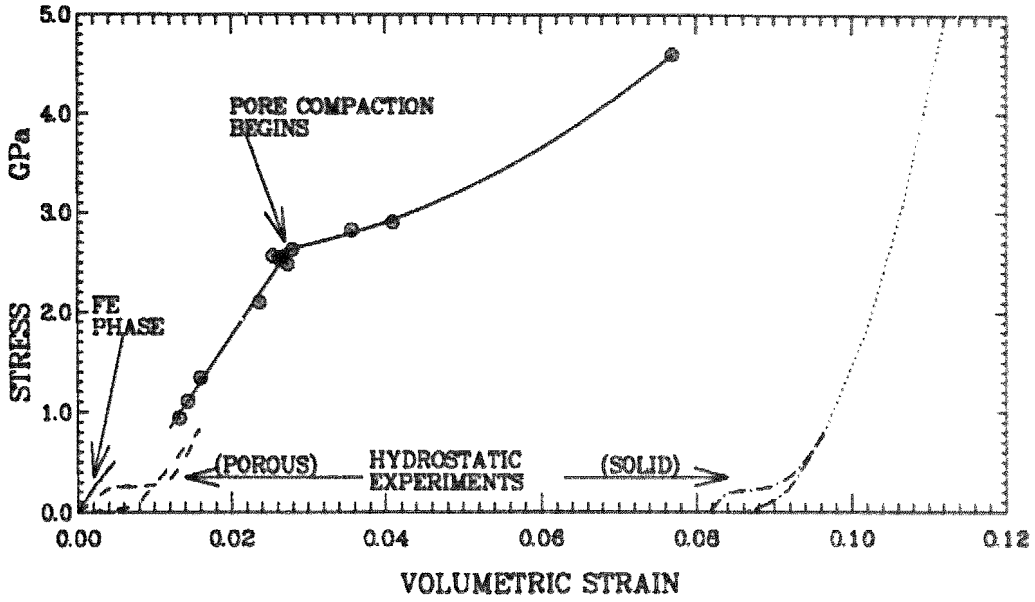

Figure 11. Hugoniot stress and strain states for PZT 95/5 determined in this investigation are shown. The results of previous hydrostatic stress-stain experiments on porous [4] and solid 95/5 PZT [24] are also shown.

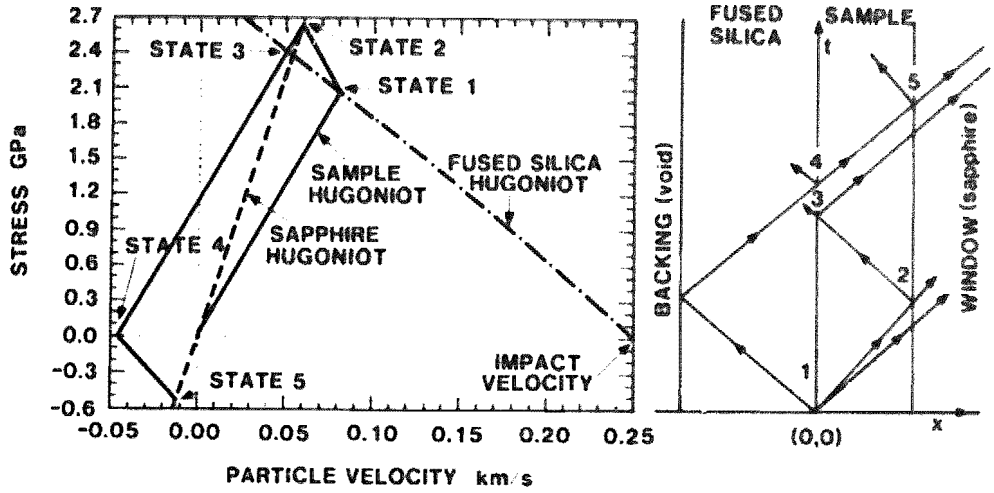

Figure 12. Lagrangian x-t and a corresponding stress *vs* velocity diagram depicting the sequence of events that occur which subsequently lead to a negative particle velocity measurement upon release at the interface in experiments FER2 and FER3.

p-u diagram, a full release will correspond to state 4 which will be measured as state 5 at the sample-window interface. It is interesting to note that in experiments FER2 and FER3, state 5 corresponds to a tension of ~ 0.5 GPa at the sample-window interface, and is essentially a measure of the interface strength between the sample and the window. The large magnitude for the interface strength is surprising, since epoxy adhesive is used to bond the window to the sample. It is conceivable that epoxy adhesives could sustain tension of that magnitude under dynamic loading conditions for durations of a few hundred nanoseconds.

A lack of rarefaction shocks [25,26] upon release in Figures 3 and 4 is indicative of sluggish reverse-transformation kinetics. These release profiles have been integrated incrementally using equations (5) and (6) to obtain the stress-strain path upon release and are indicated in Figure 13. In equations (5) and (6), c now represents the Lagrangian wave velocity of the material unloading from the shocked state. The Lagrangian wave velocity reported in Table II, represents the wave velocity of the first disturbance of the release wave traveling in the shocked material. The attenuated states for experiments FER5 and FER6 are also indicated in Figure (13) by the dotted line.

The release wave speeds plotted in Figure 14 represent the wave velocity of the first disturbance of the decompression wave traveling in the shocked material; it is usually a measure of the longitudinal sound speed, c_l ,of the material in the shocked state. As indicated in the figure, the longitudinal release wave speed of the material remains constant over the stress range of 0.9 to 2.6 GPa. Above 2.6 GPa where the pore-compaction process dominates, an increase in the longitudinal velocity with increasing stress is observed. Likewise, c_s , the shear wave speed determined from pressure-shear experiments, is a measurement of the shear wave speed of the material in the shocked state. These are determined by measuring the transit time of the shear wave indicated in Figures 5, 6, and 7, respectively. Unlike previous studies [27,28], considerable scatter is observed in the shear wave velocity profile before the primary wave arrives at the free surface. The first systematic increase in free-surface velocity profile for the transverse wave is used as a criterion to determine the arrival of the shear wave. As indicated in Figure 14, the shear wave speed is constant to within the experimental uncertainty over the same stress range. The ambient values of the wave speeds determined using ultrasonic techniques [29] are also shown in the figure. Using the relation,

$$c_b^2 = c_l^2 - \frac{4}{3}c_s^2, \tag{7}$$

the bulk sound speed, c_b, of the material in the shocked state can be calculated. Using an average value of 4.89 km/s for the longitudinal sound speed, and 2.62 km/s for the shear wave velocity, a value of 3.97 km/s is calculated for the bulk sound speed and should be valid over the stress range of 0.9 to 2.6 GPa.

3.3 Comparison With Static Experiments

The present Hugoniot measurements are shown in Figure 11. The stress-strain response of the material up to 0.5 GPa is thought to represent the material in the FE phase.

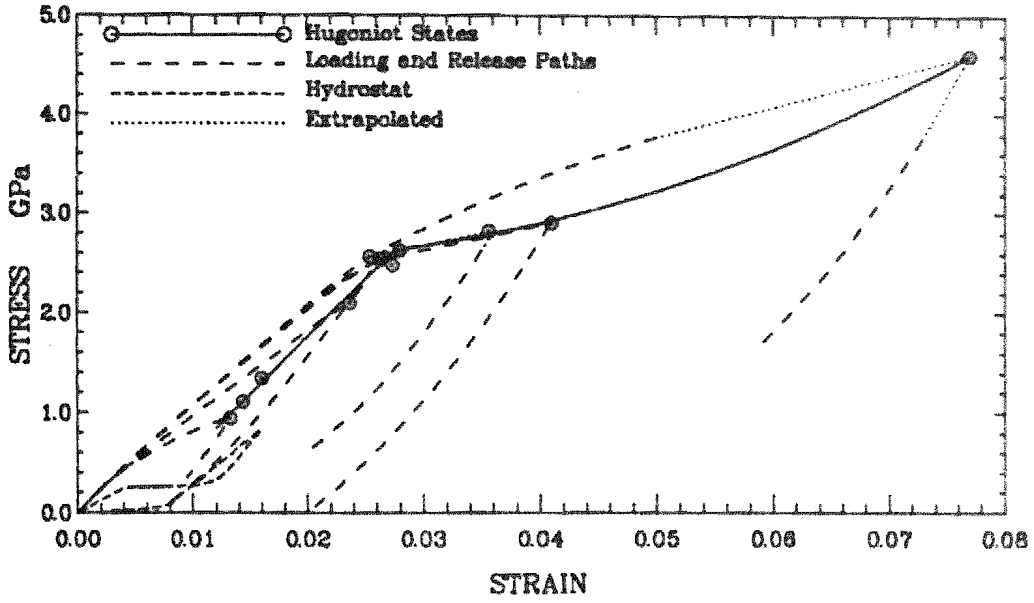

Figure 13. Shock loading and release paths indicating a remnant strain upon release. Comparison with the hydrostatic experiments suggests the existence of a mixed phase region up to 2.6 GPa. Release paths for experiments above 2.6 GPa indicate pore-compaction process to be dominant.

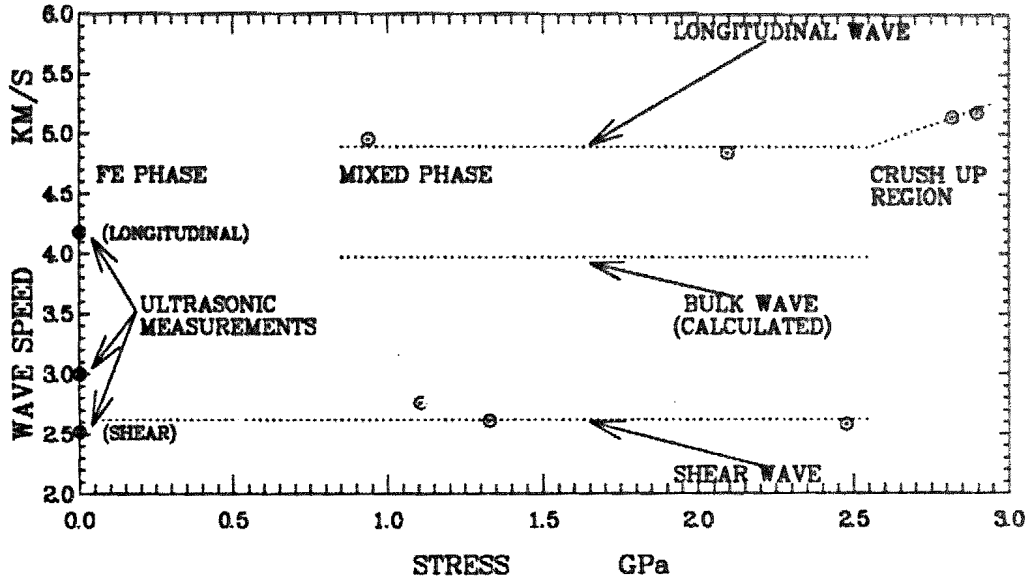

Figure 14. Variation of measured longitudinal release and shear-wave speed and calculated bulk-wave speed in the shocked state with respect to stress. Ambient pressure values determined by ultrasonic techniques are also shown.

At 0.5 GPa, there is a discontinuity, indicating a small change in volume. It appears that this discontinuity is due to both dynamic yielding and the onset of the ferroelectric-to-antiferroelectric phase change. The stress *vs* strain response of the material *in the stress range* 0.9 to 2.6 GPa can be fit with a straight line yielding the relation

$$\sigma(GPa) = -.5349 + 114.6\eta(GPa). \tag{8}$$

Thus, the slope of the line yields a sound speed of 3.96 km/s. This agrees remarkably well with the bulk sound speed estimates of 3.97 km/s, as determined from wave speed measurements (See Figure 14). Therefore, the stress-strain response of the material although represented by a straight line, should be characteristic of bulk behavior. It should not be surprising, however, that a straight line representation is adequate, since the volume change is small (1.3%) over this stress range. Above 2.6 GPa, the sudden decrease in volume with increased compression is an indication of a dominant pore compaction process occurring during dynamic loading. A comparison of the present Hugoniot measurements with the extrapolation of hydrostatic experiments on solid PZT 95/5 [24] suggests that total pore collapse would occur at approximately 8.0 GPa. The extrapolation is performed by fitting the pressure *vs* strain relation in the AFE phase to a linear least squares fit and determining its behavior at higher pressures. This, however, implicitly assumes that there are no further complications such as additional phase changes in the material behavior.

Hydrostatic pressure experiments on porous PZT 95/5 [4] are indicated in Figure 11. (The hydrostatic experiments were performed on a batch of material very similar to the one used in dynamic experiments.) As indicated in the diagram, the material transforms under hydrostatic conditions, from the FE phase to the AFE phase at $\sim$ 0.26 GPa. The resultant volume change associated with the hydrostatic phase transformation is 0.8%. When the results of the present Hugoniot measurements are compared to hydrostatic pressure measurements, it appears that on the Hugoniot, the onset of phase transformation occurs at 0.5 GPa, with a corresponding volume change associated with the phase change of $\sim$ 0.4 %(this volume change is obtained by extrapolating the linear response of the material determined over the stress region 0.9 to 2.6 GPa). Thus, the volume change associated with the phase change under dynamic loading conditions is approximately one-half of that observed under hydrostatic loading conditions, suggesting the presence of FE phase under dynamic loading. However, part of this volume change can be attributed also to dynamic yielding, and this would therefore imply even a larger fraction of FE phase. Therefore, dynamic loading conditions or the presence of shear, tends to favor the presence of FE phase. It is quite likely, therefore, that over the stress regime of 0.9 to 2.6 GPa, both phases of the material are present, with the concentration of FE phase diminishing with increasing stress.

This is further evidenced by the release paths indicated in Figure 13. The dashed lines in Figure 13 represent both the loading and release paths, as determined from the wave profiles. Note that the release states from shock states of 0.9, 2.0, and 2.4 GPa lie to the left of the static hydrostat. This would be consistent with the observation made earlier that the shock states over the stress regime 0.9 to 2.6 GPa suggest a mixed-phase state and the material is unloading along frozen mixed-phase states. One would

also expect to observe a similar release behavior if (i) upon decompression the material continuously transforms to the FE phase, and (ii) the material behavior over this stress region is elastic. The former is not likely since there is remnant strain observed upon total decompression; and the latter is not likely also, because as discussed above the stress region from 0.9 to 2.6 GPa is characteristic of the bulk response for the material. The release paths from shock states above 2.6 GPa lie to the right of the hydrostat. It is not clear, if the material is transformed entirely to the AFE phase, since the large volume changes observed at stresses over 2.6 GPa, are primarily due to pore-compaction process. In previous studies, based on charge release measurements, Lysne [5] arrived at a similar conclusion, suggesting the possibility of a mixed-phase region up to 1.6 GPa, since he found that 100% of the charge was released only above 1.6 GPa. However, since Lysne (5) was investigating poled samples, the stress states might be different.

The release paths shown in Figure 13 also seem to indicate a remnant strain upon release. This indicates a sluggish retransformation to the FE phase from the shocked state and may be the reason for the absence of rarefaction shocks upon release. It is conceivable, that for short time durations, the material does not retransform to the ferroelectric phase. Since the material is porous, it is possible that the remnant strain observed after release is also due to partial pore compaction. Both these effects are expected to be contributing, indicating a remnant strain upon release. The kinetics of reverse-phase transformation are expected to dominate below 2.6 GPa, whereas the kinetics of pore compaction are believed to be more significant above 2.6 GPa, the stress level at which the pore-compaction process is significantly initiated. This is also consistent with previous hydrostatic pressure experiments [3,4], which indicate sluggish reverse transformations. As indicated in Figure 13, under a hydrostatic-pressure environment the ceramic material exhibits a transformation from the FE phase to the AFE phase at approximately 0.28 GPa. Upon release from pressures of 0.8 GPa in the AFE phase, the material undergoes a reverse transformation at pressures lower than 0.1 GPa. Detailed X-ray diffraction analysis of recovered specimens would be necessary to determine whether the stress-induced ferroelectric-to-antiferroelectric transformation is irreversible. In addition, density measurements of recovered specimens would indicate if the remnant strain measured upon release is due to irreversible pore compaction.

3.4 Pressure-Shear Experiments

The longitudinal and transverse free-surface velocity profiles determined for the presure-shear experiments are indicated in Figures 5, 6, and 7. These correspond to longitudinal stress states of 1.1 GPa, 1.33 GPa, and 2.48 GPa, respectively. The longitudinal profiles have been discussed already in a previous section. The transverse velocity profiles shown in these figures indicate considerable premotion prior to the arrival of the main transverse wave. Previous studies on other materials [18,27,28] have not indicated a similar behavior. The apparent premotion seems to increase with increasing stress. It is possible that since the material is porous, oblique reflection of the longitudinal wave at various pore sites, would generate a shear wave internally. If the main shear wave were not present

in the material, then the time average of the shear velocity profile should net zero transverse motion. As mentioned earlier, the first systematic increase in free-surface velocity profile is used as a criterion to determine the shear wave speeds in the shocked state. The shear wave speeds determined in these experiments, seem fairly constant over the stress range of 1.0 GPa to 2.5 GPa.

The shear stress estimates obtained from these experiments are plotted as a function of mean pressure in Figure 15. Large error uncertainties in shear stress are indicated, due to the considerable premotion observed in these experiments. The shear stress estimates would depend upon the assumptions [28,30] used to determine their magnitude. A simple centered wave analysis [28] is assumed to calculate the shear stresses shown in Figure 15. Also, the shear stress estimates are expected to be a lower bound. Experimental limitations, such as slippage at the bonded interface [18] and the bond strength of alumina-filled epoxy [28,31], are expected to limit the magnitude of the shear stress transmitted into the material. However, previous studies have indicated, that at longitudinal stresses of 1.2 GPa, a shear stress wave of 0.6 GPa can be transmitted through the alumina-filled epoxy bond [28,31].

The variation of shear stress *vs* mean pressure for the FE phase is indicated in Figure 15 by the straight line. This is obtained by assuming a von Mises-type yield criterion and is calculated using

$$\sigma_x = P + \frac{4}{3}\tau, \tag{9}$$

where, τ, is the shear stress, σ_x, is the shock stress and, P, is the hydrostatic pressure. Thus, the shear stress is obtained by taking the difference between the shock stress and hydrostatic pressure shown in Figure 13. In a uniaxial strain experiment, the shear stress increases with increasing mean pressure, and when in the FE phase, develops a maximum shear stress of 0.16 GPa. At this stage, phase transformation commences, and as indicated in the figure, the shear stress stays reasonably constant while in the mixed-phase state. In particular, the plot shown in Figure 15 resembles that of a material that has undergone "plastic" deformation; i. e., the shear stress of the material increases with pressure, and upon dynamic yielding, it attains a constant value. Thus, if there is no slippage at the bonded interface, and if the measured shear stress is not being limited by the shear strength of the bond, this would suggest that dynamic yielding occurs as the material undergoes phase transformation. If the material is indeed in a mixed phase over this pressure region, as suggested by release experiments and discussed earlier, the implication is that the presence of shear seems to favor the existence of a FE phase. However, rate effects associated with the phase transformation could also be responsible for the existence of a mixed phase and, thus, cannot be ruled out completely. A pressure-temperature phase diagram for the material [2] would also suggest that any increase in temperature due to shock compression or heterogeneous deformation would favor the presence of FE phase.

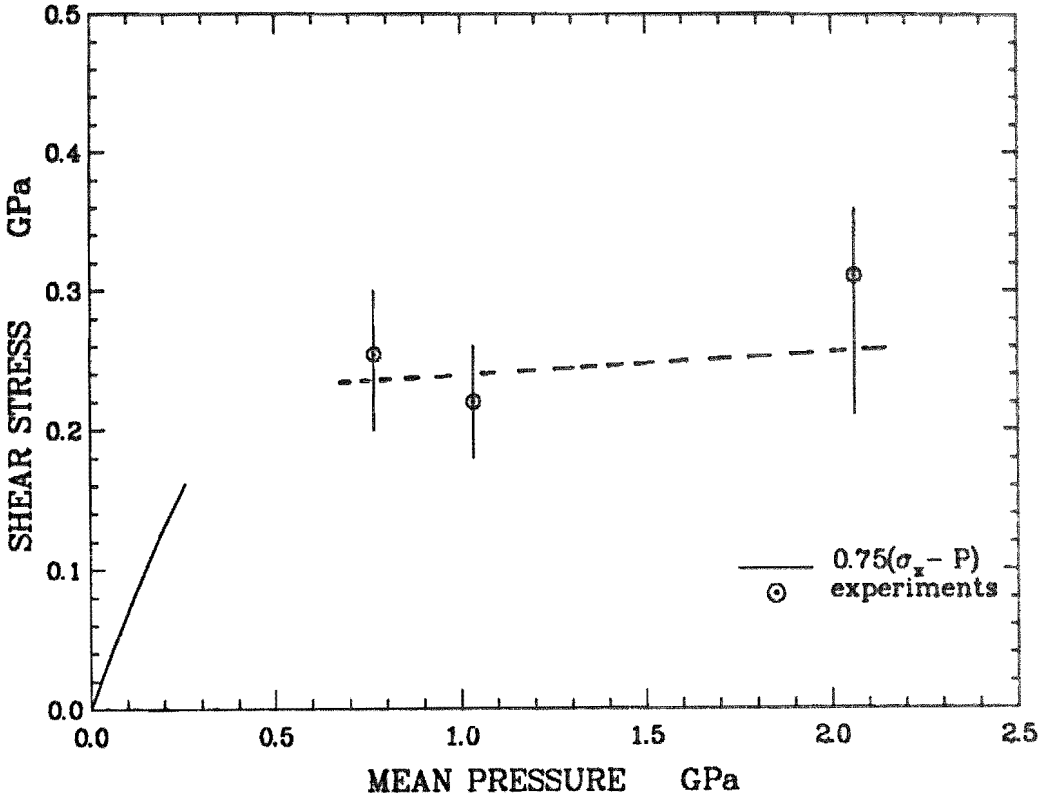

Figure 15. Variation of shear stress as a function of mean pressure as determined from these experiments.

4 Summary

To summarize, results of these experiments indicate that the onset of phase transformation to the AFE phase begins at approximately 0.5 GPa under dynamic loading conditions. Up to 0.5 GPa the dynamic stress-strain response in the ferroelectric phase has anomalous curvature, i.e. the sound speed decreases with increasing stress. Release experiments over the stress region 0.9 to 2.6 GPa indicate that the material is in a mixed phase, with the concentration of FE phase diminishing with increasing stress. Also, the kinetics of reverse-phase transformation appear to be sluggish, since residual strain is observed upon total decompression. Above 2.6 GPa, the kinetics of pore compaction and crush-up behavior dominate the mechanical response of the material. Comparison with the extrapolation of static hydrostatic experiments on fully dense material suggest that the pore-compaction process would be complete over 8.0 GPa, assuming that there are no further complications such as additional phase changes occurring in the material.

Results of pressure-shear experiments and release experiments also seem to suggest that dynamic yielding occurs at 0.5 GPa, the pressure at which the FE-to-AFE-phase transformation also commences; the phase transformation kinetics appear to be closely coupled with the dynamic yielding process and is therefore similar to the behavior of fused silica [32]. In the absence of pressure-shear and release wave experiments, one would be tempted to conclude that dynamic yielding occurs at 2.6 GPa, the pressure at which pore compaction begins. Experiments on fully dense PZT 95/5 would be necessary to conclusively verify the dynamic yield stress, since then the dynamics of the pore-compaction process would not complicate the analysis and interpretation. In addition, those experiments would be further useful in establishing a constitutive relation for the material in which the porosity is being treated as a variable.

Recovery experiments for the material over this stress range would also be useful. Detailed x-ray diffraction analysis of recovered specimens would determine whether the stress-induced ferroelectric-to-antiferroelectric transformation is irreversible, and electron microscopy techniques would help identify deformation features induced during shock-loading process. Density measurements of recovered specimens would indicate if there is permanent pore collapse upon compression.

References

1. **Neilson, F. W.**
   Effects of Strong Shocks in Ferroelectric Materials, *Bull. Am. Phys. Soc.* **2**, 302, 1957 (Abstract only).
2. **Fritz, I. J. and Keck, J. D.**
   Pressure-Temperature Phase Diagrams for Several Modified Lead Zirconate Ceramics, *J. Phys. Chem. Solids* **39**, p. 1163, 1978.
3. **Fritz, I. J.**
   Uniaxial-Stress Effects in a 95/5 Lead Zirconate Titanate Ceramic, *J. Appl. Phys.* **49**, p. 4922, 1978.
4. **Holcomb, D. J.**
   Private Communication, *Sandia National Laboratories,* (1982).
5. **Lysne, P. C.**
   Dielectric Properties of Shock-Wave-Compressed PZT 95/5, *J. Appl. Phys.* **48**, p. 1020, 1977.
6. **Lysne, P. C. and Percival, C. M.**
   Electric Energy Generation by Shock Compression of Ferroelectric Ceramics: Normal-Mode Response of PZT 95/5, *J. Appl. Phys.* **46**, p. 1024, 1977.
7. **Doran, D. G.**
   Shock-Wave Compression of Barium Titanate and 95/5 Lead Zirconate Titanate, *J. Appl. Phys.* **39**, p. 40, 1968.
8. **Dick, J. J. and Vorthman, J. E.**
   Effect of Electrical State on Mechanical and Electrical Response of a Ferroelectric Ceramic PZT 95/5 to Impact Loading, *J. Appl. Phys.* **49**, p. 2494, 1978.
9. **Reynolds, C. E. and Seay, G. E.**
   Multiple Shock Wave Structures in Polycrystalline Ferroelectrics, *J. Appl. Phys.* **32**, p. 1401, 1961.
10. **Reynolds, C. E. and Seay, G. E.**
    Two-Wave Shock Structures in the Ferroelectric Ceramics, Barium Titanate, and Lead Zirconate Titanate, *J. Appl. Phys.* **33**, p. 2234, 1962.
11. **Graham, R. A. and Asay, J. R.**
    Measurement of Wave Profiles in Shock Loaded Solids, *High Temp. High Pressures,* **10** p. 355, 1978.
12. **Asay, J. R.**
    The Sandia Shock Thermodynamics Applied Research Facility, *Sandia National Laboratories,* SAND81-1901, 1981 (unpublished).

13. **Barker, L. M. and Hollenbach, R. E.**
Shock-Wave Studies of PMMA, Fused Silica, and Sapphire, *J. Appl. Phys.* **41**, p. 4208, 1970.

14. **Barker, L. M. and Hollenbach, R. E.**
System for Measuring the Dynamic Properties of Materials, *Rev. Sci. Instrum.* **35**, p. 742, 1964.

15. **Barker, L. M. and Hollenbach, R. E.**
Laser Interferometer for Measuring High Velocities of Any Reflecting Surface, *J. Appl. Phys.* **43**, p. 4669, 1972.

16. **Amery, B. T.**
Wide-Range Velocity Interferometer, *6th Symposium on Detonation AC-R-221*, Office of Naval Research - Department of the Navy, Arlington, VA, p. 681, 1976.

17. **Barker, L. M. and Schuler, K. W.**
Correction to the Velocity Per Fringe Relationship for the VISAR Interferometer, *J. Appl. Phys.* **45**, p. 3692, 1974.

18. **Chhabildas, L. C. and Swegle, J. W.**
Dynamic Pressure-Shear Loading of Materials Using Anisotropic Crystals, *J. Appl. Phys.* **51**, p. 4799, 1980.

19. **Johnson, J. N.**
Shock Propagation Produced by Planar Impact in Linearly Elastic Anisotropic Media, *J. Appl. Phys.* **42**, p. 5522, 1971.

20. **Chhabildas, L. C., Sutherland, H. J., and Asay, J. R.**
A Velocity Interferometer Technique to Determine Shear-Wave Particle Velocity in Shock-Loaded Solids, *J. Appl. Phys.* **50**, p. 5196, 1979.

21. **Kim, K. S., Clifton, R. J., and Kumar, P.**
A Combined Normal - And Transverse - Displacement Interferometer With an Application to Impact of Y-Cut Quartz, *J. Appl. Phys.* **48**, p. 4132, 1977.

22. **Jaffe, B., Cook, W. R., and Jaffe, H**
Piezoelectric Ceramics, *Academic Press*, New York pp. 253-269, 1971.

23. **Grady, D. E.**
Processes Occurring in Shock-Wave Compression of Rocks and Minerals, *Applications in Geophysics* edited by M. H. Manghnani and S. Akimoto, Academic Press, New York, 1977.

24. **Fritz, I. J.**
Stress Effects in Two Modified Lead Zirconate Titanate Ferroelectric Ceramics, *J. Appl. Phys.* **50**, p. 5265, 1979.

25. **Duvall, G. E. and Graham, R. A.**
Phase Transitions Under Shock-Wave Loading, *Reviews of Modern Phys.*, **49**, p. 523, 1977.

26. **Chhabildas, L. C., Wise, J. L., and J. R. Asay**
Reshock and Release Behavior of Beryllium, *AIP Conference Proceedings.* **78**, p.422, 1982.

27. **Chhabildas, L. C. and Swegle, J. W.**
On the Dynamical Response of Particulate-Loaded Materials. 1 Pressure-Shear Loading of Alumina Particles in an Epoxy Matrix, *J. Appl. Phys.* **53**, p. 957, 1982.

28. Swegle, J. W. and Chhabildas, L. C.
A Technique for the Generation of Pressure-Shear Loading Using Anisotropic Crystals, *Shock Waves and High-Strain-Rate Phenomena in Metals*, edited by M. A. Meyers and L. E. Murr, Plenum, N. Y., p. 401, 1981.

29. J. H. Gelske
(Private Communication), *Sandia National Laboratories*, (1982).

30. Drumheller, D. S., Trucano, T. G., and Chhabildas, L. C.
Wavecode Constitutive Models: Particulate-Loaded Composites, *Sandia National Laboratories*, SAND84-0714, 1984, (unpublished).

31. Chhabildas, L. C.
Dynamic Transverse Particle Velocity Measurements Using Interferometric Techniques, *High Speed Photography, Videography, and Photonics*, Dennis L. Paisley, Editor, Proc. SPIE 427, p. 136.

32. Chhabildas, L. C., and Grady, D. E.
Shock Loading Behavior of Fused Quartz, *Shockwaves in Condensed Matter*, edited by J. R. Asay, R. A. Graham, and G. K. Straub, Elsevier Science Publishers, p. 175, (1984).

DISTRIBUTION:

Larry Lee
Ktech Corporation
901 Pennsylvania NE
Albuquerque, NM 87110

Sandia Internal:

1130 G. A. Samara
1131 P. J. Chen
1131 M. B. Boslough
1131 B. Dodson
1131 R. A. Graham
1131 B. Morosin
1131 R. E. Setchell
1132 I. J. Fritz
1252 D. D. Bloomquist
1510 J. W. Nunziato
1520 D. J. McCloskey
1522 R. C. Reuter
1524 K. W. Schuler
1530 L. W. Davison
1531 S. L. Thompson
1533 T. K. Bergstresser
1533 G. I. Kerley
1533 M. E. Kipp
1533 S. T. Montgomery
1533 J. W. Swegle
1533 P. Yarrington
1534 J. R. Asay
1534 L. M. Barker
1534 T. J. Burns
1534 L. C. Chhabildas (20)
1534 D. S. Drumheller
1534 D. R. Ek
1534 D. E. Grady
1534 T. G. Trucano
1534 J. L. Wise
1540 W. C. Luth
1542 B. M. Butcher
1542 L. S. Costin
1542 D. J. Holcomb
1822 K. H. Eckelmeyer
1822 M. J. Carr
1840 R. J. Eagan
1843 R. G. Dosch
1845 E. K. Beauchamp
1845 F. P. Gerstle
1845 S C. Kunz
1846 R. K. Quinn
2500 H. J. Saxton
2510 D. H. Anderson
2513 J. K. Kennedy
2513 S. A. Sheffield
2513 P. L. Stanton
2514 B. H. VanDomellen
2520 N. J. Magnani
2530 D. B. Hayes
2531 C. P. Ballard
2531 R. H. Dungan
2531 J. D. Keck
2531 W. D. Williams
2532 J. J. Marron
2532 C. T. Gebert
2560 J. T. Grissom
2561 R. A. Damerow
2561 D. K. Morgan
2561 C. E. Spencer
2564 G. E. Rochau
3141 C. M. Ostrander (5)
3151 W. L. Garner (3)
3154-4 C. E. Dalin (28)
For DOE/TIC
5163 D. F. McVey
5170 W. R. Reynolds
5172 G. C. Novotny
5173 M. J. Navratil
5341 C. E. Dalton
6240A P. C. Lysne
7472 R. H. Moore
8024 M. A. Pound